Results in Physics 52 (2023) 106864

Contents lists available at ScienceDirect

Results in Physics

journal homepage: www.elsevier.com/locate/rinp

An *in-situ* FTIR-LCR meter technique to study the sensing mechanism of MnO_2@ZIF-8/CNPs and a direct relationship between the sensitivity of the sensors and the rate of surface reaction

Lesego Malepe [a], Patrick Ndungu [b], Tantoh Derek Ndinteh [a], Messai Adenew Mamo [a,c,1,*]

[a] *Department of Chemical Science, University of Johannesburg, PO Box 17011, Doornfontein, 2028 Johannesburg, South Africa*
[b] *Department of Chemistry, University of Pretoria, Private Bag X20, Hatfield 0028, Pretoria, South Africa*
[c] *DST-NRF Centre of Excellence in Strong Materials (CoE-SM), University of the Witwatersrand, Johannesburg, Johannesburg 2000, South Africa*

ARTICLE INFO

Keywords:
Diethylamine
Solid-state sensor
MnO_2@ZIF-8
Carbon soot
ZIF-8

ABSTRACT

Diethylamine vapor is harmful to people if inhaled or swallowed, as it results in the oxidation of hemoglobin in the body into unwanted methemoglobin, which is unable to transport oxygen in the blood, resulting in reduced blood oxygenation. Lack of blood oxygenation leads to hypoxemia. MnO_2 nanorods, carbon soot, and MnO_2@ZIF-8 are sensing materials used to prepare solid-state gas sensors that operate at room temperature. The prepared sensing materials were characterized by scanning electron microscopy, transmission electron microscopy, powder X-ray diffraction, X-ray photoelectron spectroscopy, and Fourier-transform infrared spectroscopy. The performance of the MnO_2@ZIF-8 based sensor improved significantly when the carbon soot was introduced into the composite. The effect of the amount of CNPs in the composite on the performance of the sensors was studied. The MnO_2@ZIF-8/CNPs-based sensor with a 3:1 mass ratio was highly selective towards diethylamine vapor over acetone, methanol, ethanol, and 3-pentanone vapors. An *in situ* FTIR coupled with LCR meter was used to understand the sensing mechanism of diethylamine vapor and it was found that the sensing mechanism was by deep oxidation of diethylamine to CO_2, H_2O, and other molecules. The sensing mechanism was studied by monitored by CO_2 band intensity which was produced from the reaction between the sensing materials and the analyte vapor. As the sensor's exposure time increased the intensity of the CO_2 IR band increased. We observed the direct relationship between the surface reaction rate and the sensor's sensitivity.

Introduction

Volatile organic compounds (VOCs) are organic compounds that are easily vaporized at room temperature, even at low concentrations [1]. Highly volatile VOCs, including basic alcohols, amines, ketones, and aldehydes, often have low molecular weights, boiling points, and high vapor pressures [2]. Diethylamine is an amine compound with a molar mass of 73.14 g/mol and a boiling point of approximately 55 °C. It is a volatile organic compound (VOC) that is widely used in pesticides, dyes, pharmaceuticals, corrosion inhibitors, and herbicides. Exposure to diethylamine may cause serious damage to the human skin, eyes, and respiratory systems [3,4]. The inhalation of amines is also reported to oxidize hemoglobin from the body system into unwanted methemoglobin, which can distribute oxygen throughout the body; however, methemoglobin cannot [5]. Accidental leakage of diethylamine in working environments may result in human health discomfort. However, there are very few scientific articles on diethylamine vapor detection, highlighting the need for a device to monitor diethylamine vapor within the atmospheric working area. A wide range of semiconductor metal oxides (SMOs), including tin oxide (SnO_2) [6], titanium dioxide (TiO_2) [7], zinc oxide (ZnO) [8], tungsten trioxide (WO_3) [9], and manganese dioxide (MnO_2) [10], have received significant attention from researchers and engineers for application in chemiresistive gas sensors owing to their low cost, ease of synthesis, good stability, good sensitivity, and large surface-to-volume ratio. MnO_2 is a transition-based metal oxide that possesses wide morphological flexibility and exists in many crystallographic polymorphs, including α-, β-, χ-, δ-, and ε-polymorphs [10–12]. Owing to their relative abundance and free toxicity,

---

* Corresponding author at: Department of Chemical Science, University of Johannesburg, PO Box 17011, Doornfontein, 2028 Johannesburg, South Africa.
E-mail address: messaim@uj.ac.za (M.A. Mamo).

[1] ORCID: 0000-0002-6734-2051.

https://doi.org/10.1016/j.rinp.2023.106864
Received 29 June 2023; Received in revised form 30 July 2023; Accepted 14 August 2023

they are used in many applications, including water treatment, catalysis, energy storage, and gas sensors [12]. The synthesis of MnO_2 has received considerable attention owing to its controllable dimensions, morphology, pore size, and surface-to-volume ratio. MnO_2 nanostructures, including nanosheets, nanorods, nanoparticles, nanotubes, nanospheres, and nanowires, have been reported to exhibit activity in catalysis and sensing applications [13]. Although there are many MnO_2 nanostructures, recent reports by Okechukwu et al. have shown that the MnO_2 nanorods have high sensitivity toward the detection VOCs [14]. There are major drawbacks to SMOs gas sensors, which have poor selectivity towards the gas of interest, and they operate at relatively high temperatures above 150 °C [13–15]. Applying high temperatures to the sensor film leads to structural instability, resulting in a poor sensor lifespan. Introducing carbon materials into MnO_2 nanostructures improves the electrical conductivity and surface-to-volume ratio, leading to fast response-recovery times and gas sensitivity [14]. Inexpensive carbon nanoparticles (CNPs) from candle soot are promising materials for application in gas sensors because of their good surface-to-volume ratio, good electrical conductivity, nanosize, high sensitivity, and fast response-recovery times. The source of CNPs soot is the burning of household candle soot in the presence of atmospheric molecules [16,17]. The sensitivity and selectivity towards detecting the targeted gas from pure SMOs, carbon materials, and SMO-based gas sensors can be improved by introducing zeolitic imidazolate frameworks (ZIFs) owing to their porosity tunability [18].

ZIFs are a subclass of metal–organic frameworks with tetrahedral arrangements made up of metal cations and imidazole as an organic linker, with a geometry such as ZIF-8 consisting of zinc ions and 2-methylimidazole. ZIF-8 have small pore apertures (3.4 Å) and large cavities (11.6 Å) and are reported to be hydrophobic, and possess good chemical and thermal stabilities [19,20]. ZIFs, such as ZIF-8, are mostly used in gas storage, separation, sensing, and purification of small molecules because of their tunable pore sizes [21]. Although ZIF-8 possesses unique properties for gas sensors, to date, there have been only a few reports on ZIF-8 gas sensors because of their poor electrical conductivity; thus, they operate at temperatures between 180 and 400 °C, have poor regeneration ability, and there is no evidence of oxidation of the analytes on pure ZIFs sensors [18–21]. Because MnO_2 only provide sensing interactions at relatively high temperatures due to their poor electrical conductivity, introducing good conducting CNPs soot on MnO_2@ZIF-8 improves the electrical conductivity, resulting in the sensors working at relatively low temperatures. We propose using a ternary composite of MnO_2, ZIF-8, and CNPs to detect diethylamine at room temperature (approximately 25 °C. Detecting diethylamine using MnO_2@ZIF8/CNPs sensors would be energy efficient, highly selective towards diethylamine, durable, and block moisture interference (humidity).

Experimental section

Synthesis of MnO_2 nanorods

The MnO_2 NRs were synthesized using the hydrothermal method reported by J. Zhang et al. Firstly, 0.63 g of $KnMO_4$ and 0.25 g $MnSO_4$ were dissolved in 40 mL of deionized water. The resulting solution was stirred for 30 min to obtain a homogeneous purple solution. The solution was transferred into a 100 mL Teflon-lined stainless steel autoclave, and the hydrothermal process was carried out at 160 °C for 12 h. After the reaction, the autoclave was allowed to cool to room temperature. The dark brown precipitate was washed several times with deionized water and ethanol by centrifugation and dried at 80 °C [22].

Synthesis of MnO_2@ZIF-8

Typically, 0.10 g MnO_2 NRs, 0.20 g $Zn(NO_3)(H_2O)_6$, and 0.80 g 2-methylimidazole were dissolved in 40 mL of methanol [23]. The mixture was constantly stirred for 2 h at room temperature, and the precipitate was collected via centrifugation. The dark brown precipitate obtained was washed several times with ethanol and dried at 60 °C for 12 h.

Prepared of CNPs

The preparation of carbon nanoparticles (CNPs) was done following the reported method by Malepe L et al. [17]. The pyrolysis of light candles prepared the CNPs, and a ceramic crucible was placed approximately 1 cm above the burning candle to collect soot. After sufficient accumulation of carbon soot, a spatula was used to scrape the product, which was then stored in a vial until further use.

MnO_2@ZIF-8/CNPs composite

MnO_2@ZIF-8 and the CNPs were added together to form a MnO_2@ZIF-8/CNPs composite via physical mixing. 0.6 g of MnO_2@ZIF-8 and 0.3 g of CNPs were dissolved in 20 mL of N, N-dimethylformamide. The mixture was sonicated for 15 min and the homogeneous mixture was magnetically stirred at room temperature for 12 h. Subsequently, the product was dried at 80 °C for 12 h (Fig. 1).

Gold-plated-interdigitated electrode and sensor

The sensor was prepared by drop-coating the prepared material onto a gold-plate interdigitated electrode. The electrode was designed to have 0.1 mm width spacing between the gold lines and was counted to be 18 pairs of 7.9 mm long (see supporting document Fig. S1). The electrodes were washed with ethanol and dried at room temperature before use.

Gas-sensing setup and sensor testing

The electrical characterization of the fabricated sensor investigations was performed using a Keysight E4980A LCR meter connected to the fabricated sensor and the computer via electrical wires, as presented in Fig. 2. A voltage of 0.5 alternating current was supplied to the prepared sensor at an optimal relative frequency of 25 KHz [24], and the LRC meter, diaphragm vacuum pump, and computer were all connected to a 230 V power source. The sensor was placed inside a sealed 20 L round-bottom flask connected to a vacuum pump to remove the exposed gas and reform oxygen adsorbates by allowing atmospheric air to come into contact with the sensor. MnO_2 nanorods, ZIF-8, and CNPs are the sensing materials used to fabricate sensors to detect diethylamine. The prepared and tested sensors include sensor 1 (CNPs), sensor 2 (MnO_2), sensor 3 (MnO_2@ZIF-8), sensor 4 (MnO_2@ZIF-8/CNPs with a mass ratio 1:1), sensor 5 (MnO_2@ZIF-8/CNPs with mass ratio was mass ratio 2:1) and sensor 6 (MnO_2@ZIF-8/CNPs with a mass ratio 3:1). As the sensing materials, MnO_2@ZIF-8 was taken as a primary composite, and MnO_2@ZIF-8/CNPs was taken as secondary composite. Sensor 4, sensor 5, and sensor 6 were prepared by varying the mass of the primary composite (MnO_2@ZIF-8) in the secondary composite, whereby CNPs were kept constant. Other sensors tested from our laboratory to support our experiments include MnO_2/CNPs, all at a mass ratio of 1:1. The mass ratio of the MnO_2@ZIF-8/CNPs was varied from 10 to 20 and 30 mg in the preparation of sensors 4, 5, and 6, respectively. All sensors with a 1:1 mass ratio were prepared by mixing 10 mg and 10 mg of their respective materials and dissolving them in 10 mL of DMF. The mixtures were stirred overnight and 10 μL was drop-coated onto the interdigitated gold electrodes.

The prepared sensors were allowed to dry in atmospheric air and subsequently placed in a vacuum desiccator for two weeks to remove any remaining DMF from the sensors. All prepared sensors were tested on five analytes: methanol, ethanol, acetone, 3-pentanone, and diethylamine vapor. One analyte was tested at a time, wherein volumes (1, 2, 3, 4, and 5 μL) were injected into a 20 L round bottom flask at a time. The

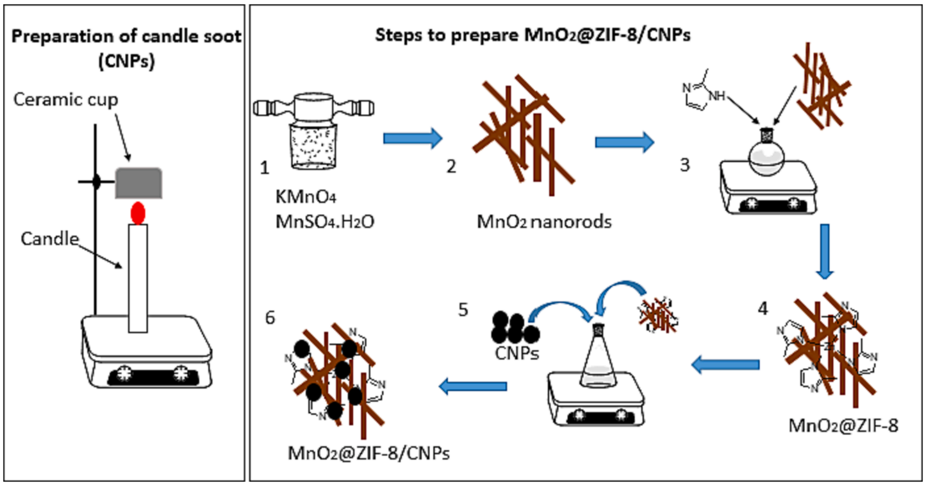

Fig. 1. Schematic illustration of the preparation of candle soot (CNPs) and MnO2@ZIF-8/CNPs.

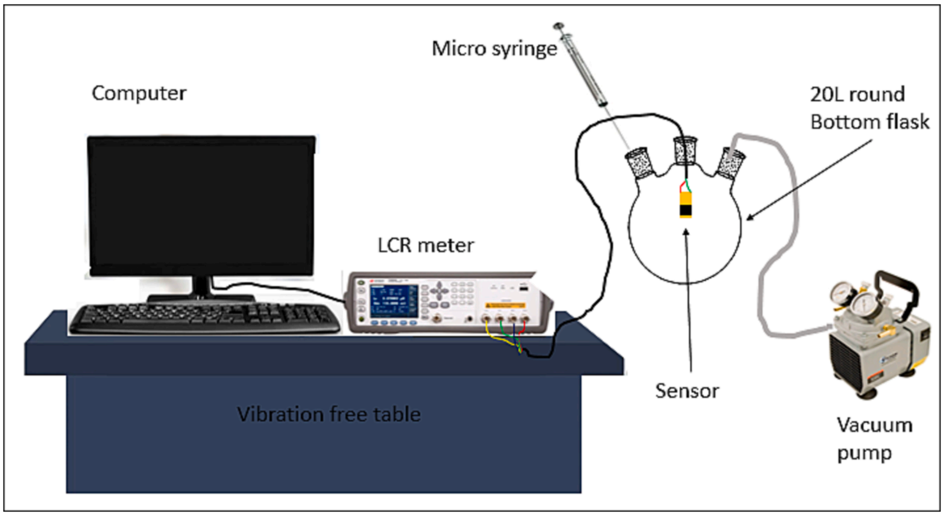

Fig. 2. Gas sensing setup.

contact between the injected analyte and the prepared sensor was 10 min, and the vapor was removed using a vacuum pump that ran at atmospheric pressure by sucking air into the volume chamber (20 L round bottom flask). Subsequently, the sensor was allowed to rest for 3 min before injection. The concentrations of the injected analytes were calculated using the following formula:

$$C = \frac{22.4\,pTV_s}{273\,M_rV} \times 1000,$$

Where C represents the vapor concentration, p and Mr represent the density and the molecular mass of the analytes, respectively. V_s is the volume injected, and V is the volume of the chamber [25].

Sensor response and recovery tests

The response time is the time taken by the sensor to reach the plateau of the maximum response. The time taken by the sensor to return to its baseline during analyte vapor removal from contact with the sensor is referred to as recovery time. In this study, the response time was recorded as 90% of the maximum response when the analyte was in contact with the sensor, and the recovery time was measured as 90% before the sensor reached its baseline. The electrical responses of the prepared sensors to the target gas were reported as the relative resistance (ΔR) and defined as

$$\Delta R = R_{gas} - R_{air} \tag{1}$$

Selectivity test

Firstly, one mL of each of the five analytes (diethylamine, methanol, ethanol, 3-pentanone, and acetone) was mixed to make five mL. From the mixture, 5 μL of aliquot were tested to investigate the selectivity of diethylamine using the setup shown in Fig. 2.

In Situ FTIR coupled with LCR meter setup and testing

The prepared sensor was placed on the upper wall of a cylindrical glass cell with a volume of approximately 110 mL and closed on both ends using KBr windows. The sensor is electrically connected to an LCR meter (Fig. 3). The cell was placed at the center of the FTIR sample compartment, wherein the IR beam passed through KBr windows that closed the cell. Before the gas analyte was injected into the gas cell, the sensor was run for about 180 min, a pre-injection period. During the In Situ measurement, approximately 20 ppm of diethylamine vapor was introduced into a cylindrical cell. The LCR meter measured the sensor’s electrical response (resistance), and the FTIR spectra were collected every 2 min.

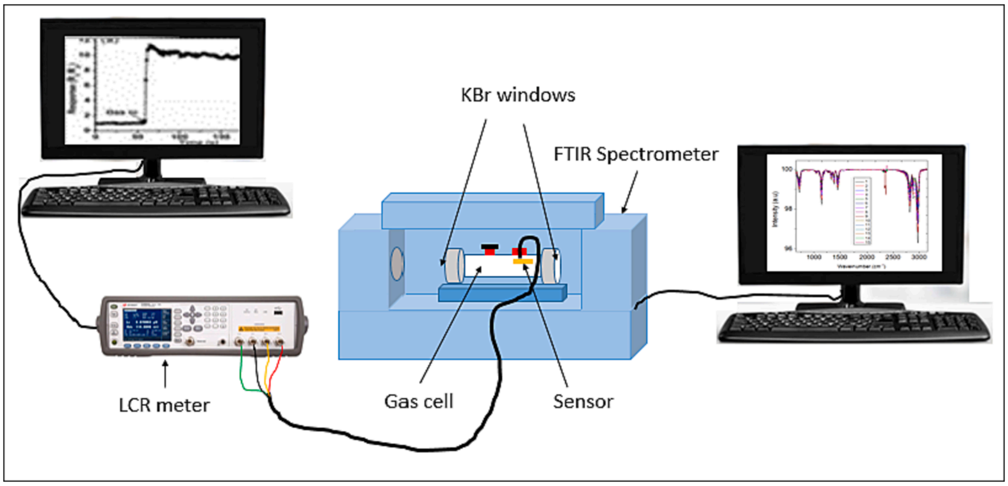

Fig. 3. Schematic illustration of in-situ FTIR coupled with an LCR meter to study the sensing mechanism.

Curve fitting for the infrared CO_2 band

The area under the curve was obtained using magic plot software on a selected region of the CO_2 band bending at 673–660 cm^{-1} on the IR bands. The area was obtained using a Gaussian function for the 6 spectra of the sensors.

Characterization techniques

Samples were analyzed on a JEOL-TEM 2010 (Japan) high-resolution transmission electron microscope (HR-TEM) at an acceleration voltage of 200 kV using the Gatan software. TEM sample preparation, the sample was dispersed in ethanol and DMF (1:3), wherein the mixture was drop coated on Holey carbon-coated copper grids. The Holey carbon-coated copper was allowed to dry with the sample before use. Scanning electron microscopy (SEM) was performed at 30 kV using a FEI Nova Nanolab 600 FEG-SEM. SEM pin mounts specimen were used to spray our samples on it, and further carbon coated them before analysed. Structural analysis was revealed using powder X-ray diffraction (PXRD), Bruker D2 Phaser using LynxEye detector with radiation of a CuKα at a wavelength of 0.154 nm and Bruker Senterra laser Raman spectrometer fitted with frequency-doubled Nd-YAG laser with the wavelength of 532 nm. X-ray photoelectron spectroscopy (XPS; XSAM800, Kratos, Manchester, UK) was used to determine the oxidation state and elemental composition. The XPS used Al Kα (1487 eV) radiation as an excitation source, an average of 40 scans, time 1 min 17 s, 0.20 eV. Fourier transform infrared spectroscopy (FTIR, PerkinElmer Spectrum 100) was used to determine the sensing mechanism and characterize the materials by studying their functional groups. For sample preparation, solid samples of about 5 mg were mixed together with about 0.8 g of potassium bromide (KBr). The mixture was grinded using a pestle and mortar and the FTIR solid pellet was created using the pressed pellet technique.

Results and discussions

SEM was used to examine the surface morphologies of all the synthesized materials. The CNPs were spherical in structure and showed a

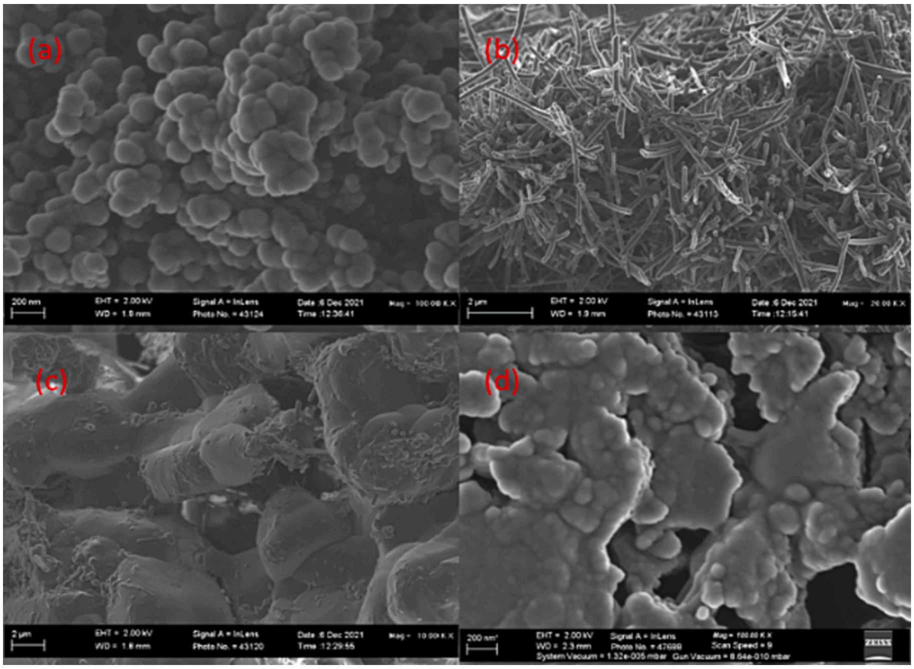

Fig. 4. SEM image of (a) CNPs, (b) MnO_2 NRs, (c) MnO_2@ZIF-8 and (d) MnO_2@ZIF-8/CNPs.

high degree of agglomeration, as shown in the SEM image in Fig. 4a. The spheres were stacked on top of each other, forming nano-structured lumps. Fig. 4b shows a representative SEM image of the hydrothermally synthesized MnO_2 nanorods (NRs), where MnO_2 is a one-dimensional longitudinal rod. The surfaces of the MnO_2 rods were smooth and uniform, and the rods crossed each other without any uniform arrangement. The SEM image of the synthesized MnO_2@ZIF-8 is shown in Fig. 4c. The external roughness of MnO_2@ZIF-8 resulting from the attachment of MnO2 rods was covered by CNPs spheres (see Fig. 4d). SEM-energy dispersive X-ray (EDX) was used to identify the elemental compositions of the CNPs, MnO_2, MnO_2@ZIF-8, and MnO_2@ZIF-8/CNPs composites (see the supporting document Fig. S2). The EDX profile revealed that the CNPs contained approximately 94.7 % carbon and 5.3 % oxygen.

The EDX profile of the MnO_2 sample has Mn 74.1 % and 25.9 % of oxygen. The EDX profile in Fig. S2c shows that MnO_2@ZIF-8 elemental composition was 45 % oxygen, 27.7 % Zn, 15.9 % Mn, and 12.0 % N. The MnO_2@ZIF-8/CNPs sample contained C, Zn, Mn, O, and N; further confirmation was performed by XPS analysis.

The internal morphologies of MnO_2, CNPs, MnO_2@ZIF-8, and MnO_2@ZIF-8/CNPs were studied using high-resolution transmission electron microscopy (HR-TEM). MnO_2 is a longitudinal rod with a

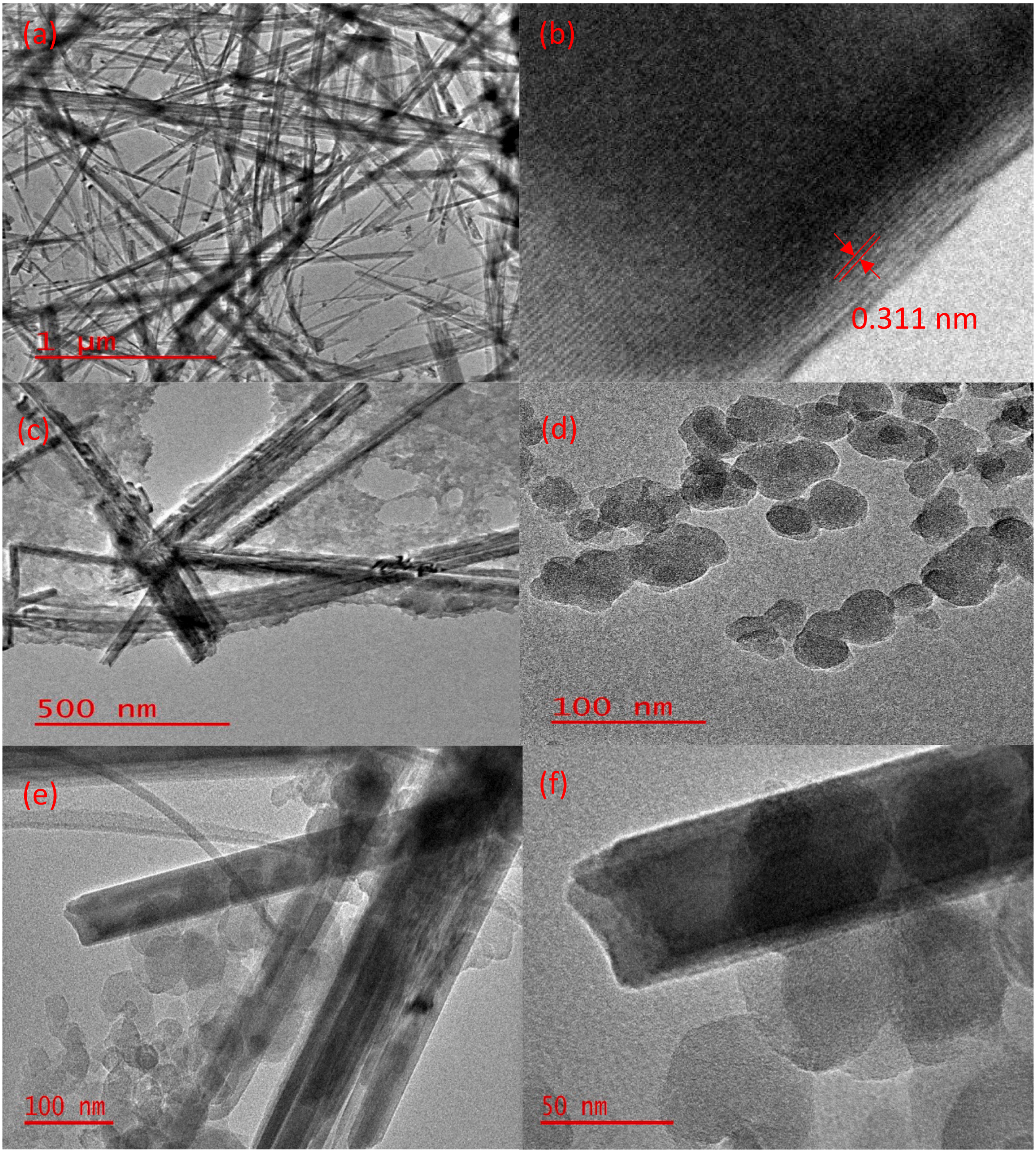

Fig. 5. HR-TEM image of (a-b) MnO_2 NRs, (c) MnO_2@ZIF-8, (d) CNPs, (e-f) MnO_2@ZIF-8/CNPs.

23–56 nm diameter, and the rods are randomly arranged (see Fig. 5a). Fig. 5b shows a MnO_2 lattice spacing of 0.311 nm, corresponding to the crystal plane (301). The crystal plane corresponds well with the XRD results (see Fig. 6b). The TEM image of MnO2@ZIF-8 (see Fig. 5c) shows that ZIF-8 is a thin sheet with MnO_2 attached to it. The TEM image in Fig. 5d reveals that the CNPs are chain-linked spheres that agglomerate. The particle size of the CNPs was in the range of 14–52 nm. The TEM image of the MnO_2@ZIF-8/CNPs composite reveals that the CNPs are randomly attached to the MnO_2 NRs, and some edges of the ZIF-8 sheet-like structure (see Fig. 5e). Fig. 5f shows the magnified area of the MnO_2@ZIF-8/CNPs composite, wherein MnO_2 NR surrounded the CNPs, and some CNPs were stacked on top of the rod.

Powder X-ray diffraction (PXRD) was done to study the structures of candle soot (CNPs), MnO_2, MnO_2@ZIF-8, and MnO_2@ZIF-8/CNPs, as shown in Fig. 6. The XRD pattern of the CNPs shows two predominant peaks positioned at $2\theta = 24.5°$ and 43.7°, which are attributed to the amorphous nature and graphitic structure of the CNPs [2]. The XRD pattern of the MnO_2 nanorods (Fig. 6b) shows peaks at $2\theta = 12.4°$, 18.1°, 28.8°, 37.5°, 41.6°, 49.7°, 56.2°, 60.0°, 65.2°, 69.4°, and 72.7° corresponding to the (110), (200), (310), (211), (301), (411), (600), (521), (002), (541), and (222) planes [JCPDS no. 044-0141], ascribed to tetragonal α-MnO_2 [26]. The presence of new XRD peaks added to MnO_2 in Fig. 6c shows 9.5°, 10.7°, 12.7°, and 16.1°, corresponding to the (011), (002), (112), and (013) planes, respectively [27], indicating the successful synthesis of ZIF-8 on MnO_2 NRs. Two broad peaks of the CNPs were observed in the XRD pattern of MnO_2@ZIF-8, proving the successful preparation of MnO2@ZIF-8/CNPs through physical mixing (see Fig. 6d). Fig. 6(e-i) presents the FTIR spectra of the CNPs, 2-methylimidazole, MnO_2@ZIF-8, MnO_2, and MnO_2@ZIF-8/CNPs to study their chemical bonding nature. As shown in Fig. 6e, the FTIR spectra exhibited a broad peak at 3452 cm^{-1}, representing O-H stretching. The 2864 and 2935 cm^{-1} peaks corresponded to C-H bonds from aldehydes and simple C-H bonds or carboxylic O-H bonds, respectively. The peak at 1636 cm^{-1} represents C=C stretching, whereas the peak at 1384 cm^{-1} corresponds to the CH_3 group and O-H stretching. The bands at the lower end of the wavenumber region, including 663 cm^{-1} and 1017 cm^{-1}, correspond to sp^2 and sp^3 from the aromatics of amorphous CNPs [28]. The peaks at 683, 754, 1119, 1322, 1474, and 1606 cm^{-1} were attributed to the aromatic ring of 2-methylimidazole (see Fig. 6f). The peaks detected at 531 cm^{-1} and 998 cm^{-1} of the MnO_2@ZIF-8 FTIR spectra confirm the bond between Zn and N. The peak observed at 672 cm^{-1} is ascribed to O-Mn-O stretching, the peak at 1384 cm^{-1} is attributed to O-H stretching, and the broad peak at 3452 cm^{-1} is ascribed to the presence of absorbed H-O-H molecules, as shown in Fig. 6h [29]. Fig. 6i presents the FTIR spectrum with major peaks at 3452, 2935, 2864, 1636, 1384, 998, and 754 cm^{-1}, confirming the presence of MnO_2, CNPs, and ZIF-8 in the MnO_2@ZIF-8/CNPs composite.

X-ray photoelectron spectroscopy (XPS) analysis revealed the elemental content, the oxidation state of the metals, and the oxygen species available on the sensing materials. The XPS full survey scan of the CNPs has confirmed the presence of carbon and oxygen atoms (see Fig. 7a). The MnO_2@ZIF-8 and MnO_2@ZIF-8/CNPs survey scans show Zn 2p, Mn 2p, N 1s, O1s, and C 1s peaks, indicating the elemental existence of zinc (Zn), manganese (Mn), nitrogen (N), oxygen (O), and carbon (C) (see Fig. 7b and 7c). For the CNPs, the O 1s XPS spectrum shows only O_γ and O_β oxygen-reactive species (see Table 1), but the MnO_2@ZIF-8 and MnO_2@ZIF-8/CNPs have additional alpha oxygen (O_α). Generally, for metal oxides and semiconductor materials, O_α is ascribed to the lattice oxygen, O_β represents the adsorbed oxygen species, and O_γ is due to an adsorbed hydroxyl group (–OH) on the surface of the material (see Fig. 7d-f) [30]. After the composites were formed by mixing the sensing materials, the total reactive oxygen species of the MnO_2@ZIF-8/CNP, O_γ, and O_β increased significantly. The presence of highly reactive oxygen species, particularly gamma oxygen (O_γ) and beta oxygen (O_β), on the surface of sensing materials, plays an important role in the sensing mechanism [2,17]. The Zn 2p XPS spectrum in Fig. 8a displays two peaks at 1022.0 and 1045.4 eV which are attributed to Zn 2p $_{3/2}$ and Zn 2p $_{1/2}$, respectively. The difference in the binding energies of the two, which was 23.4 eV, indicated the existence of Zn^{2+} in MnO_2@ZIF-8. The Mn 2p XPS spectrum in Fig. 8b presents two peaks at 642.0 and 653.6 eV, respectively, with a difference in the binding energy of 11.6 eV confirming the existence of Mn^{2+} in MnO_2 [31]. N 1s spectrum of MnO_2@ZIF-8 and MnO_2@ZIF-8/CNPs in Fig. 8c-d showed that there are three peaks positioned at 399.0, 400.0, and 406.6 eV which are assigned to N-C, N-Zn and N=C bonds, respectively [32]. The XPS peak assigned to the N-Zn bond confirms the successful synthesis of ZIF-8 by the successful coordination of zinc metal and nitrogen.

Sensing performances

The electrical characteristics of all the prepared sensors were

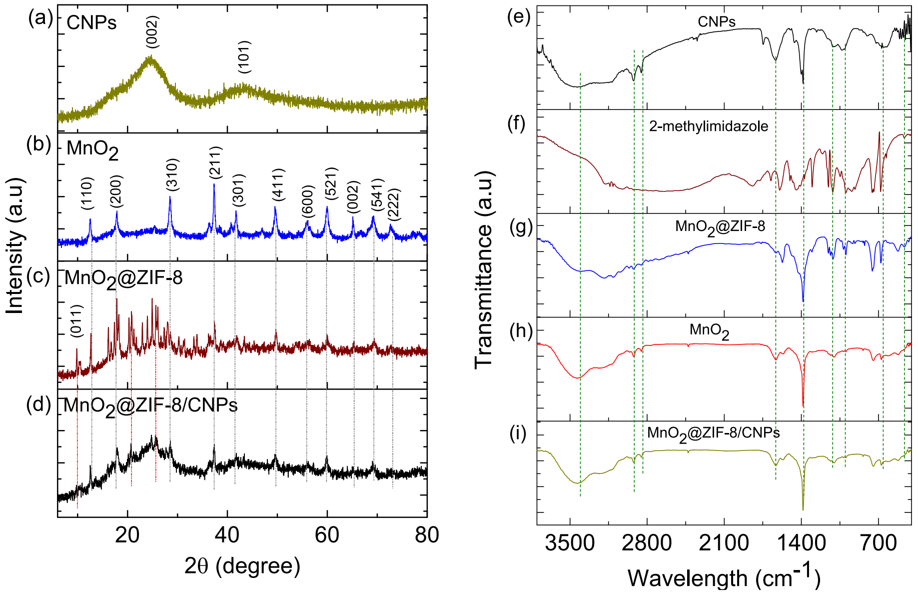

Fig. 6. XRD patterns of (a) CNPs, (b) MnO_2 NRs, (c) MnO_2@ZIF-8, (d) MnO_2@ZIF-8/CNPs, the FTIR spectra of (e) CNPs, (f) 2-methylimidazole, (g) MnO_2@ZIF-8, (h) MnO_2, and (i) MnO_2@ZIF-8/CNPs.

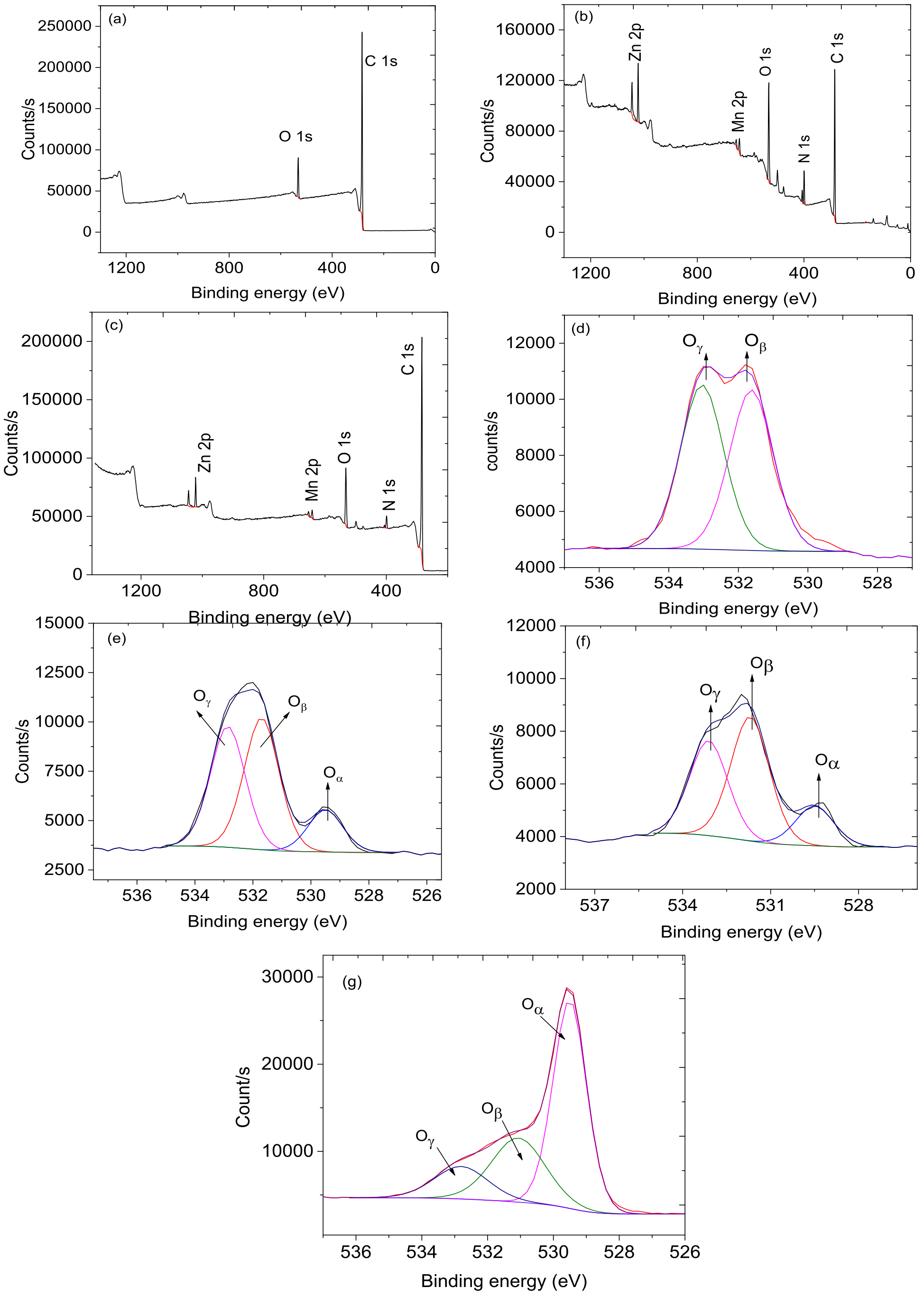

Fig. 7. XPS survey spectra of (a) CNPs (b) MnO_2@ZIF-8, (c)MnO_2@ZIF-8/CNPs, XPS 1 Os spectra of (d) CNPs, (e) MnO_2@ZIF-8, (f) MnO_2@ZIF-8/CNPs and (g) MnO_2.

Table 1
Calculated oxygen percentages of the materials from XPS graphs.

CNPs		MnO_2		MnO_2ZIF-8		MnO_2ZIF-8/CNPs	
Peak position at	Atomic % of oxygen	Peak position at	Atomic % of oxygen	Peak position at	Atomic % of oxygen	Peak position at	Atomic % of oxygen
$O_\alpha \rightarrow 529.3$	0	$O_\alpha \rightarrow 529.4$	53	$O_\alpha \rightarrow 529.4$	11	$O_\alpha \rightarrow 529.3$	11
$O_\beta \rightarrow 531.7$	53	$O_\beta \rightarrow 530.9$	34	$O_\beta \rightarrow 532.1$	76	$O_\beta \rightarrow 532.0$	73
$O_\gamma \rightarrow 533.1$	47	$O_\gamma \rightarrow 532.9$	13	$O_\gamma \rightarrow 533.4$	13	$O_\gamma \rightarrow 533.5$	16

evaluated at room temperature with an average relative humidity of approximately 40% during the detection of methanol, ethanol, acetone, 3-pentanone, and diethylamine vapor. The three sensing materials were used to fabricate the sensors; MnO_2, CNPs, and MnO_2@ZIF-8, which were prepared by either neat or combining the sensing materials and varying the masses of the composites, therefore sensor 1 (only CNPs),

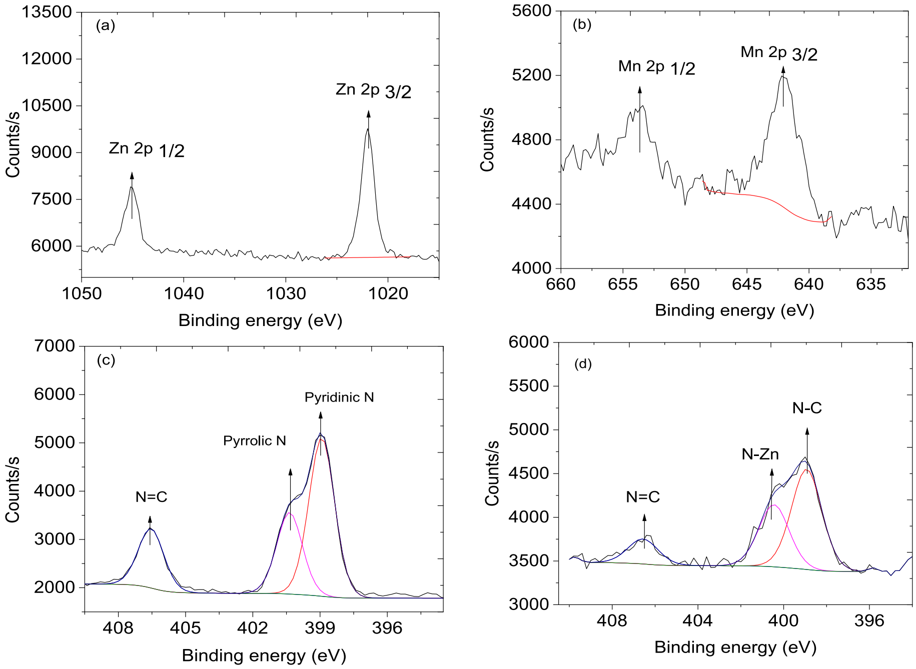

Fig. 8. XPS spectra of (a) Zn 2p of MnO_2@ZIF-8, (b) Mn 2p of MnO_2@ZIF-8, (c) N 1s of MnO_2@ZIF-8, and (d) N 1s of MnO_2@ZIF-8/CNPs.

sensor 2 (only MnO_2), sensor 3 (only MnO_2@ZIF-8), sensor 4 (MnO_2@ZIF-8/CNPs with a mass ratio of 1:1), sensor 5 (MnO_2@ZIF-8/CNPs with mass ratio with a mass ratio of 2:1), and sensor 6 (MnO_2@-ZIF-8/CNPs with a mass ratio of 3:1). The relative change in resistance (ΔR) was recorded for all fabricated sensors during testing the performance of the sensors.

Among the prepared sensors, the MnO_2 NRs sensor did not show any meaningful change in the sensor response during exposure to analyte vapors at low concentrations; however, at high concentrations, the sensor responded (See Fig. S3). All the remaining sensors responded well to the targeted analyte during the exposure and recovered extremely well to their baseline after removing the analyte vapor from the chamber, which is a good indication of the sensors' self-regeneration ability. As indicated earlier, plain MnO_2 NRs as an active sensing material were not responsive; however, when ZIF-8 was incorporated with MnO2 using a one-pot synthesis method to synthesize MnO_2@ZIF-8 as an active sensing material, and the sensor exhibited a response. This improvement was due to the synergistic effect of the two sensing materials, which increased the percentages of O_γ and O_β after MnO_2@ZIF-8 formed (See Table 1).

Using CNPs as a sensing material has advantages over other sensing materials, such as fast recovery, good stability, lower signal-to-ratio, and the ability to improve the sensitivity of the sensors [17]. Possession of such excellent properties would increase the performance of the sensors. For the detection of diethylamine vapor, we used variable mass ratios of MnO_2@ZIF-8 to CNPs in the composites; for example, sensor 4 (MnO_2@ZIF-8/CNPs with a mass ratio of 1:1), sensor 5 (MnO_2@ZIF-8/CNPs with mass ratio with a mass ratio of 2:1), and sensor 6 (MnO_2@-ZIF-8/CNPs with a mass ratio of 3:1). It can be seen from Fig. 9 that at the first injection, at a concentration of 11.82 ppm, there was a noticeable increase in the relative responses from approximately 0.75, 8.3, and 150 Ω. This shows that the amount of MnO_2@ZIF-8 within the composite sensors plays a crucial role in improving the sensing response. The sign of the responses has changed as we increase the amount of MnO_2 in the composites. At a 1:1 mass ratio, the sensor behaved as a p-type with the reducing gas diethylamine vapor, although, MnO_2 is an n-type semiconductor. However, as the amount of MnO_2 increases, the behaviour changes to n-type and the conductivity of the sensors increases as the concentration of the analyte increases. The reduced electron-depletion layer thickness and potential barrier increase the sensor's conductivity.

The sensor with a higher MnO_2@ZIF-8 content had a relatively fast response-recovery time, and the sensor with a lower MnO_2@ZIF-8 content was slow to respond and recover (Table 2 and Fig. 10). The response and recovery times of the sensors are reported based on the time required to achieve 90% response and recovery.

Sensitivity, selectivity, and repeatability. The sensitivity of the gas sensors during the detection of vapor analytes was taken from the gradient of the calibration curves for relative resistance (ΔR) vs concentration (C) and it was determined using the formula $S=\frac{\Delta R}{\Delta C}$ [17]. The calculated sensitivities of the analyte vapors to their respective sensors are summarized in Table S1. It was observed that the sensitivities of the materials, namely, CNPs, MnO_2 NRs, and MnO_2-CNPs were extremely low for all the tested vapor analytes, whereas MnO_2@ZIF-8 and the MnO_2@ZIF-8/CNPs composites showed better sensitivity. The sensitivity of the MnO_2@ZIF-8/CNPs composites increased with an increase in the MnO_2@ZIF-8 content within the composite (Fig. 11a). Sensor 6 was highly sensitive to diethylamine vapor, with a sensitivity of 5.49 Ωppm^{-1} and very poor sensitivity to ethanol vapor (0.0001 Ωppm^{-1}). Thus, among all the sensors prepared and tested for all the selected vapors, sensor 6 was the best for the detection of diethylamine vapor with high sensitivity.

Selectivity is one of the most important parameters in sensor functionality. The sensor can detect the target analyte from interference vapors and only shows the sensing response of the targeted vapor analyte. Therefore, sensor 6 was selected as the best sensor for the selectivity test. The targeted analytes were methanol, ethanol, acetone, 3-pentanone, and diethylamine mixed vapors response and the individual analyte vapor responses were compared (see Fig. 11b). The analytes were prepared by mixing 1 mL of each analyte (methanol, ethanol, acetone, 3-pentanone, and dimethylamine vapors) to obtain 5 mL of the analyte mixture. Then from the 5 mL of the mixed analyte, 5 μL was injected into a 20 L round bottom flask (chamber), and sensor 6 was exposed to mixed analyte vapor. The sensor response was 176 Ω for the mixed analytes, and the pure diethylamine analyte vapor response was 151 Ω (Fig. 11b). The mixed analyte response is only 14% of that of pure diethylamine; this increment is due to interference mainly from acetone, which is the second most sensitive analyte. Nevertheless, the sensor

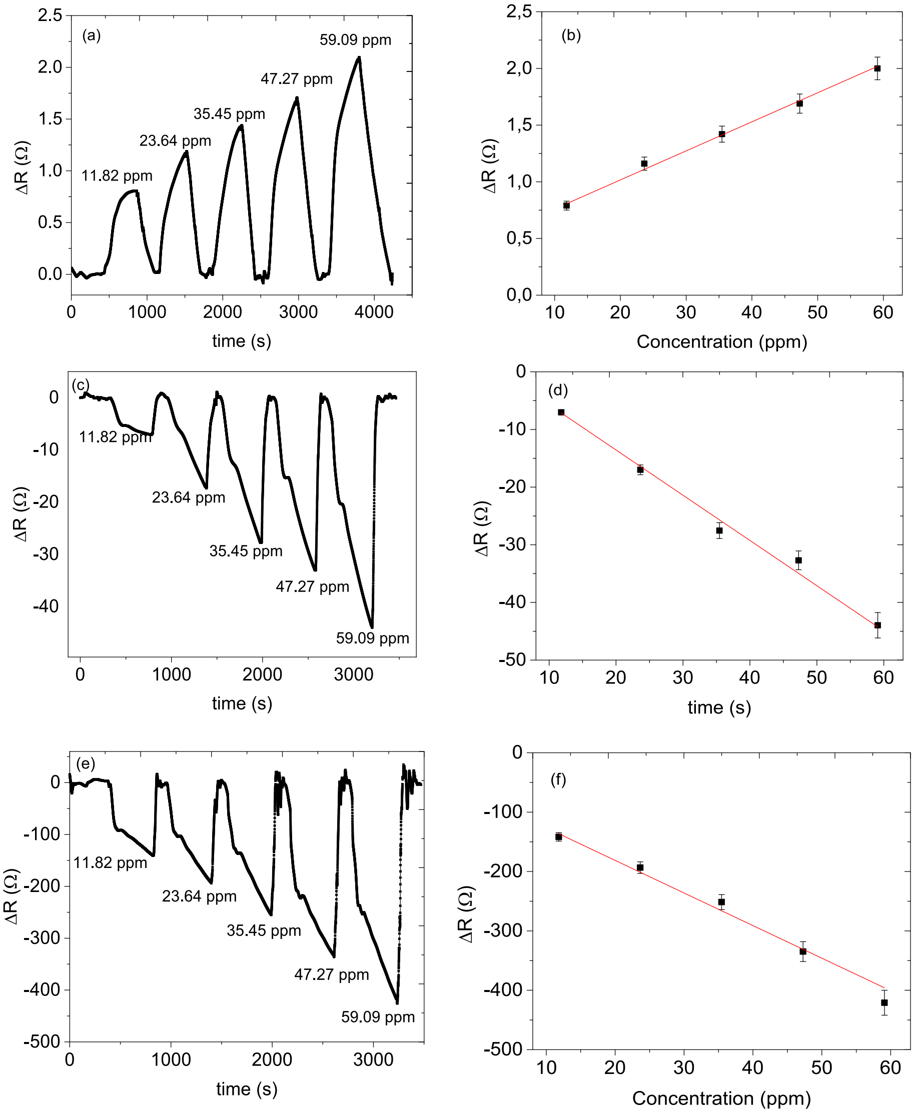

Fig. 9. Dynamic response as a function of time at different concentrations of diethylamine vapor on (a and b) sensors 4, (c and d) sensor 5, and (e and f) sensor 6 and their respective response calibration curves.

Table 2
Response and recovery times of the sensors during the detection of diethylamine vapor.

Sensors	Response time (s)	Response time (s)
Sensor 4	164	191
Sensor 5	87	45
Sensor 6	67	22

response for the mixed analyte is close to the pure diethylamine vapor. Therefore, it is possible to say that our sensor can selectively detect the targeted analyte.

The repeatability of gas sensors is another critical parameter because it shows the stability of the sensors after several exposures to the analyte vapor, in which the sensor can reproduce the same reading for the same concentration under the same conditions over time [33,34]. In real applications, there is a need for a sensor that reproduces the same reading over time. Thus, sensors 5 and 6 reusability studies were performed to detect diethylamine vapor by injecting 47.27 ppm of diethylamine vapor for five consecutive cycles for each sensor. The maximum response was found to be approximately 33.95 ± 0.40 Ω and 329.19 ± 9.26 Ω respectively (see Fig. 11c-d). The sensor responses were approximately 90% the same in magnitude, and the sensors returned to their baseline after gas removal, showing the sensors' good stability and reusability.

Humidity

Exposing a gas sensor to different relative humidity conditions is an important factor to investigate because, in many cases, most sensors exhibit a constant change in relative humidity during real-time applications [35,36]. Changes in atmospheric relative humidity can result in more than a 50% change in the sensor's performance [37]. Thus, a sensor that provides slight changes at different relative humidities is still considered good. However, the main aim was to obtain a sensor that was unaffected by humidity conditions. Hence, our best-performing sensor, 6, was investigated in the relative humidity (RH) range of 39% to 60% during the detection of diethylamine vapor. Specifically, 11.82 ppm of diethylamine vapor was used and detected for three trials at relative humidities of 44%, 55%, and 64%, and the maximum response was found to be 154, 161, and 183 Ω, respectively (see Fig. 12a). An increase in relative humidity from 44 to 64 % results in a slight increase in gas response, which could result from water molecules trapped on the surface of the gas sensor. The sensor maintained the same shape but was tested under different humidity conditions. However, the response of the

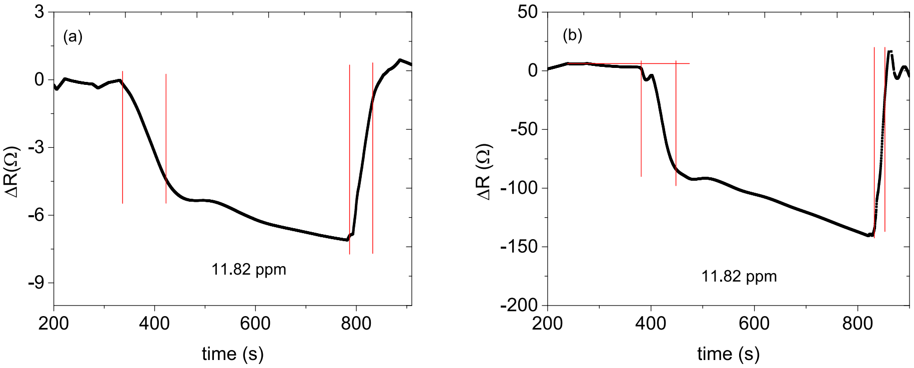

Fig. 10. Response recovery times of sensors 5 (a) and 6 (b) during the detection of diethylamine vapor.

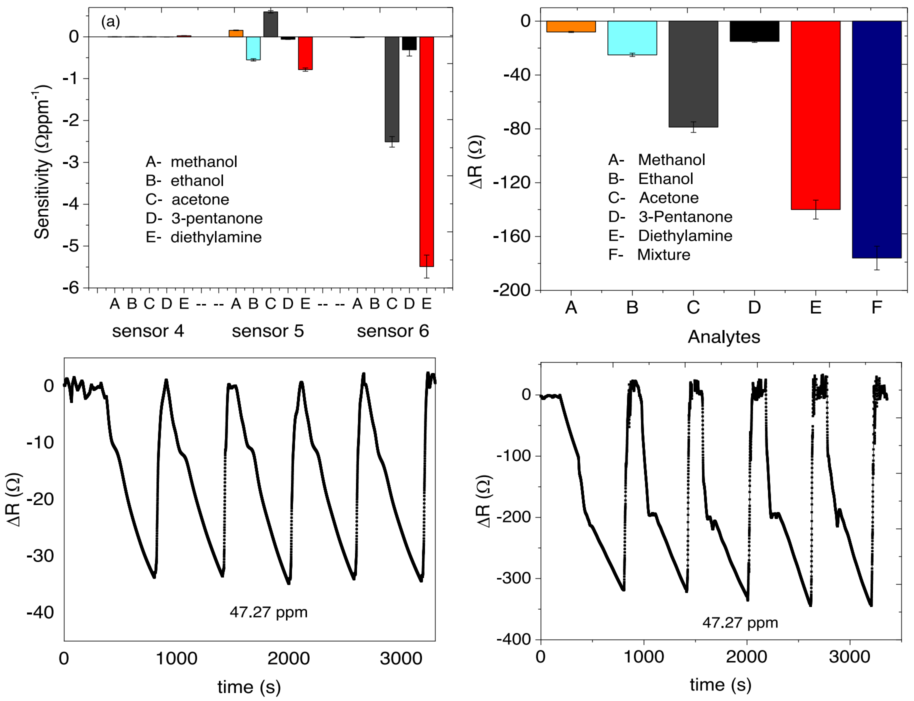

Fig. 11. (a) Comparative sensitivity of analytes on sensors, (b) comparative vapor response of the mixture vapor and individual analytes, (c) repeatability graph of sensor 5, and (d) sensor 6 on diethylamine.

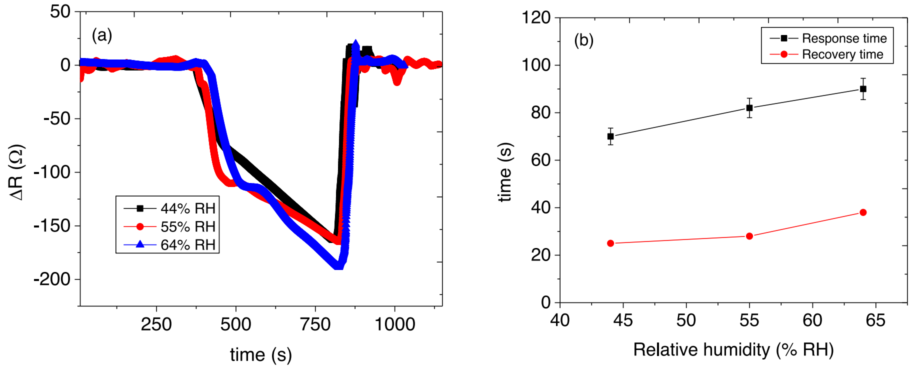

Fig. 12. (a) Humidity investigation of sensor 6 and (b) response-recovery time under different humidity conditions.

sensor significantly changed at greater than 85% RH (the result is not shown here). Interestingly, with an increase in humidity conditions from 44 to 64 % RH, the response time during the detection of diethylamine vapor increased from 72 s to 90 s, and the recovery time changed from 25 s to 38 s (see Fig. 12b).

Limit of detection

The limit of detection (LOD) in gas sensors is the minimum possible vapor concentration a gas sensor can detect. The LOD of sensor 6 for the detection of diethylamine vapor was quantified. The relationship between concentrations from 11.82 ppm to 59.09 ppm and electrical response under the resistance parameter was linear with a gradient of 5.49 Ωppm^{-1} and the correlation coefficient (R) is 0.98 (see Fig. 9f). The formula used to calculate the detection limit is as follows: LOD = 3 × RMS/slope [38], where the RMS is the standard deviation with a value of 0.001. From the calculations, the LOD of sensor 6 for detecting diethylamine vapor is 5.5 ppb. Sensor 6 could detect diethylamine vapors at extremely low concentrations (ppb level).

Sensing mechanism

Different sensing materials show different sensing mechanisms; various polymers have different sensing mechanisms. However, the most dominant sensing mechanisms are electrostatic between the interaction of electron reach polymer, for example, nitrogen-containing backbone and electron-deficient analyte molecules, polarization, Lewis acid and base interactions between the analyte molecules and the polymer [39,40]. On the other hand, the interaction between the adsorbed analyte molecules leads to the swelling of the polymer, thus increasing the overall volume and pushing away the polymer chains from one another; this causes a change in the sensors' conductivity [41]. In the case of carbonaceous materials, the dominant accepted sensing mechanism is charge transfer between carbonaceous nanomaterials and molecules adsorbed on their surface [42]. In a recent report, the presence of reactive oxygen species on the carbonaceous materials, the Oγ, and Oβ, do have similar sensing mechanisms as SMO [14,16,17]. The generally accepted sensing mechanism for SMO is once the organic analyte molecules are adsorbed on the surface of the SMO, the reactive oxygen on the SMO's surface reacts and converts the analyte molecules into CO_2 and H_2O.

Based on the gas response behavior of the MnO_2@ZIF-8/CNPs (on sensor 6), the composite exhibits the characteristics of a p-type semiconductor during the detection of vapor analytes. Incorporating CNPs into MnO_2@ZIF-8 forms a p-n heterojunction because CNPs behave like p-type semiconductors. Therefore, the excellent performance of the MnO_2@ZIF-8/CNPs is due to the p-n heterojunction formed at the interfaces. The advantage of heterojunction formation is that electrons can easily transfer from the MnO_2@ZIF-8 into the CNPs to form enough oxygen vacancies on the surface of MnO_2@ZIF-8. The p-n heterojunction also helps to increase the electronically charged oxygen vacancies, leading to an increase in the conductivity of the composite. The formation of heterojunctions also helps adsorb more oxygen molecules to form extra active sites, eventually capturing electrons from MnO_2@ZIF-8. During the sensor's exposure to the analyte, the oxygen ions react with the target gas molecules [43] (See Table 1).

It is worth mentioning that when a heterojunction is formed, the sensors' semiconductor behavior depends on the sensing materials' dominant behavior, either p- or n-type semiconductors. For example, sensor 4 (MnO_2@ZIF-8/CNPs with a mass ratio of 1:1) is dominated by the CNPs semiconductor character, n-type (see Fig. 12), with similar behavior to the CNPs sensor. When the mass of MnO_2@ZIF-8 was increased, the CNPs were kept constant (see sensors 5 and 6), and the gas-sensing behavior changed from n-type to p-type semiconductor behavior. This is due to the dominant material (MnO_2@ZIF-8), the p-type (see Fig. 12).

On the surface of the sensing materials, the adsorbed oxygen molecules react with the sensing materials to form a depletion layer and turn oxygen molecules into highly reactive species (O_2^{2-}, O_2^-, and O^-) [44–46]. Generally, most carriers in n-type semiconductor metal oxides are electrons. Thus, electrons are extracted from such materials when exposed to an oxidizing gas, leading to increased resistance. In p-type semiconductor metal oxides, however, holes are the majority carriers during sensing [47]. In p-type sensing materials, the adsorbed oxygen molecules form a hole accumulation layer. The holes are extracted from the p-type semiconductor metal oxide when exposed to an oxidizing gas (acceptor), decreasing resistance.

For the diethylamine molecule, ethyl ($-CH_2CH_3$) is an electron-donating group and the electron cloud density on the nitrogen atom increases during the interaction of the analyte and the sensing material [48]. The resistance increases with the vapor concentration when the diethylamine molecules interact with the CNPs sensor and sensor 4. However, when sensors 5 and 6 were exposed to analyte vapor, the sensors' resistance decreased as the diethylamine concentration increased. Although the MnO_2@ZIF-8-based sensor response was relatively small in magnitude during exposure to vapor, introducing the CNPs in the composites significantly improved the sensor response. This is due to the presence of oxygen molecules in the carbon soot (CNPs) (see Table 1), which are converted into reactive oxygen species during sensing [49]. The EDX results confirmed that the CNPs contained approximately 5.3% oxygen. The XPS analysis (see Fig. 7) also confirmed the oxygen species formed during the pyrolysis reaction in the presence of atmospheric oxygen.

The *In-situ* FTIR coupled with an LCR meter method was used for sensors based on CNPs, MnO_2@ZIF-8/CNPs (1:1 mass ratio), MnO_2@ZIF-8/CNPs (2:1 mass ratio), and MnO_2@ZIF-8/CNPs (3:1 mass ratio) to study the sensing mechanism of gaseous diethylamine. During the *in-situ* FTIR coupled with the LCR meter connected to a chosen sensor measurement, the relative sensing response was recorded simultaneously the FTIR spectra were taken every two minutes. The intensity of CO_2 IR bands at 668 cm^{-1} and 2349 to 2277 cm^{-1}, the bending and asymmetric stretching mode, respectively [50,51], were used to monitor the surface reaction. The intensity of the CO_2 IR bands continued to grow as the diethylamine vapor exposure of the sensor increased, as shown in Figs. 13 and 14. It is observed that the CO_2 bending shows a single peak, indicating pure CO_2, while CO_2 asymmetric shows doublet peaks, which could be a mixture of CO_2, H_2O, and/or carbon monoxide [52]. The CO_2 formation is due to the deep oxidation of diethylamine vapor on the surface of the sensing materials, and CO_2 molecules diffuse from the sensing material. At $t = 2$ min, the CO_2 band intensities were very weak for all the sensors, but as the exposure time increased, the CO_2 bands became intense.

We observed that the intensity of the CO_2 band increased when the sensing materials formed heterojunctions; for example, the intensity of the CO_2 IR band in the case of CNPs increased when MnO_2@ZIF-8 /CNPs were formed. This could be related to the increased reactive oxygen species on the surface of the sensing materials when the composite was formed (Table 1). Furthermore, the amount of MnO_2@ZIF-8 in the composites affects the intensity of the CO_2 band (see the inset of Fig. 13a–d). All sensors underwent deep oxidation of the dimethylamine vapor to carbon dioxide and other small molecules, such as H_2O and NO_2; even the pure carbon soot sensor showed the same decomposition mechanism, the analyte into CO_2 (See Fig. 13a inset). To understand the relationship between the sensitivity, surface reaction rate, and CO_2 band intensities, we employ the area under the CO_2 curve at 668 cm^{-1} using Gaussian curves from 2 to 12 min of exposure. The plotted curve of the areas under the curve of the CO_2 bends at 668 cm^{-1} against time (Fig. 14), and their slopes were compared to the sensitivity. The gradient can be assumed as the reaction rate on the sensing material. Therefore, the sensor's sensitivity is directly proportional to the reaction rate on the surface of the sensing material, as summarized in Table 3. For example, the best-performing sensor, the 3:1 mass ratio of MnO_2@ZIF-8/CNPs, recorded the highest value of 0.0776 of the area under the curve with respect to time. This indicates a parameter that can be used to measure the sensor performance directly related to the sensor's sensitivity.

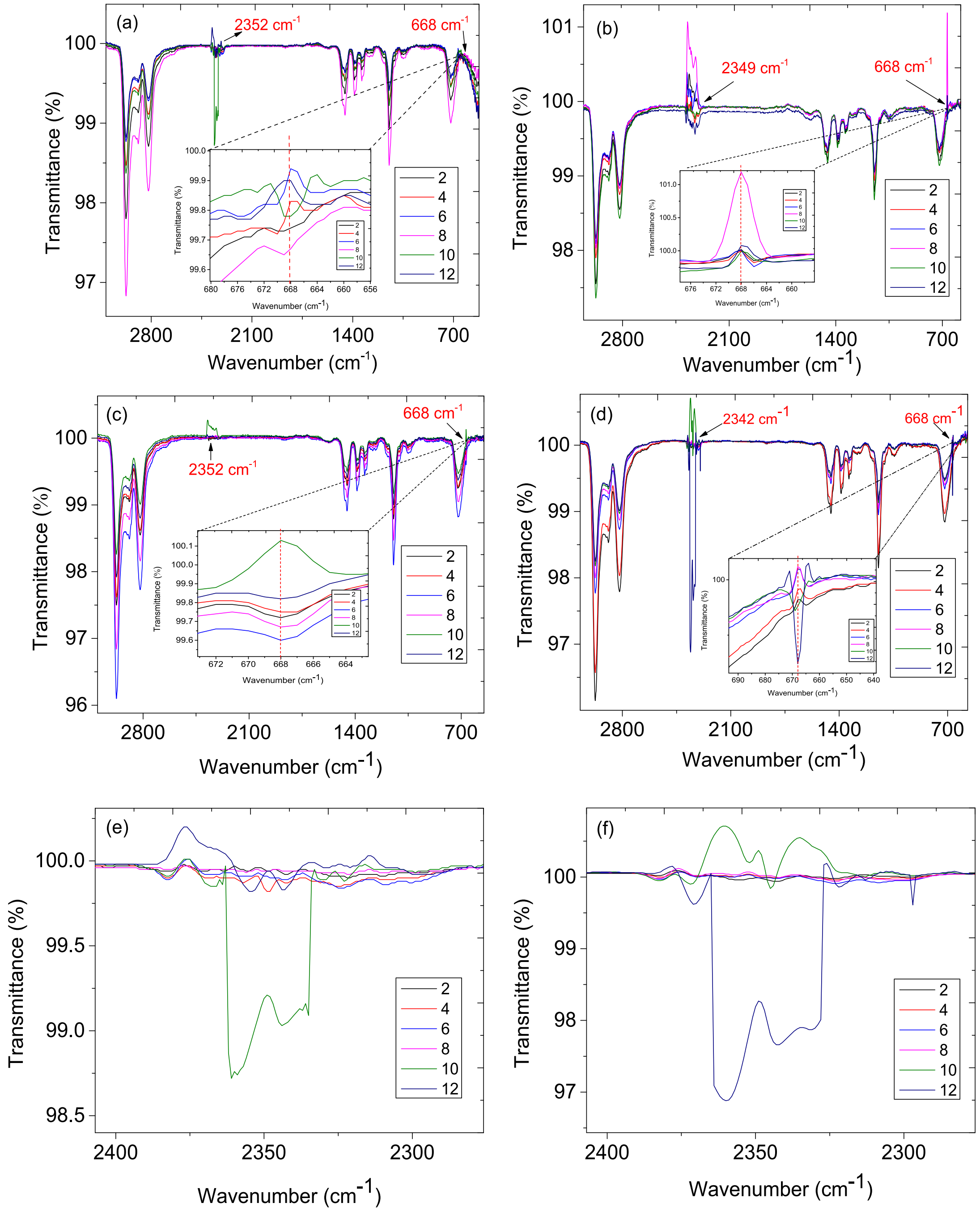

Fig. 13. In situ FTIR spectra on diethylamine vapor (a) CNPs, (b) sensor 4, (c) sensor 5, and (d) sensor 6, and a narrow region of asymmetric CO_2 bands for CNPs sensor and sensor 6.

Conclusion

In summary, MnO_2 NRs, carbon soot, MnO_2@ZIF-8, and MnO_2@ZIF-8/CNPs were successfully prepared and fully characterized using SEM, HR-TEM, FTIR, PXRD, and XPS. The prepared materials were used to fabricate solid-state gas sensors, and MnO_2@ZIF-8/CNPs with a mass ratio of 3:1 (named sensor 6) was highly sensitive and selective for detecting diethylamine vapor over acetone, methanol, ethanol, and 3-pentanone vapors. Sensor 6 recorded 5.5 ppb as the detection limit, and our sensor showed fast response-recovery times of 67 s and 22 s. The fabricated sensor was also minimally affected by changes in humidity. The *in situ* FTIR coupled with an LCR meter method was used to study the sensing mechanism of sensor 6 interacting with diethylamine vapor. The sensor mechanism was by decomposition of the analyte vapor on the surface of the sensing material to CO_2 and other molecules. This was confirmed by monitoring the intensity of the CO_2 bands at around 2350 and 668 cm^{-1}. The CO_2 IR band intensity at 668 cm^{-1} as the contact time between the sensor and analyte progresses. Furthermore, the sensor's sensitivity is directly proportional to the sensing materials' surface reaction rate.

Author Contributions

All authors contributed equally.

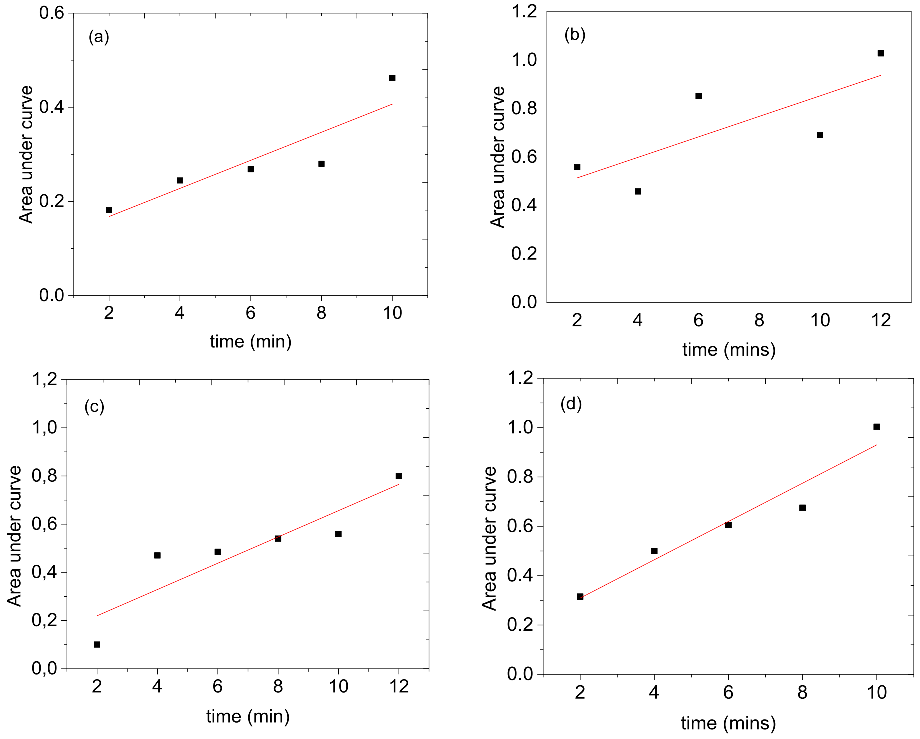

Fig. 14. Calibration curves of the area under the curve of CO_2 IR band intensity at 668 cm^{-1} against time for the (a) CNPs sensor, (b) sensor 4, (c) sensor 5, and (d) sensor 6.

Table 3
Relationship between sensor sensitivity and gradient of the area under the curve of CO_2 versus time.

Sensor	Sensitivity (Ω/ppm)	The slope of CO_2 IR intensity (ΔA/Δt)
CNPs	0.0029	0.0298
MnO_2@ZIF-8/CNPs (1:1)	0.0256	0.0423
MnO_2@ZIF-8/CNPs (2:1)	0.7850	0.0545
MnO_2@ZIF-8/CNPs (3:1)	5.4900	0.0776

Funding Sources

We thank the University of Johannesburg, South Africa for its financial assistance.

CRediT authorship contribution statement

Lesego Malepe: Conceptualization, Investigation, Methodology, Data curation, Formal analysis, Software, Visualization, Writing – original draft. **Patrick Ndungu:** Resources, Supervision, Formal analysis, Investigation, Validation, Visualization, Writing – review & editing. **Tantoh Derek Ndinteh:** Resources, Supervision, Formal analysis, Investigation, Validation, Writing – review & editing. **Messai Adenew Mamo:** Conceptualization, Investigation, Methodology, Resources, Supervision, Project administration, Data curation, Formal analysis, Funding acquisition, Validation, Visualization, Writing – review & editing.

Declaration of Competing Interest

The authors declare that they have no known competing financial interests or personal relationships that could have appeared to influence the work reported in this paper.

Data availability

Data will be made available on request.

Acknowledgment

All the authors acknowledge the University of Johannesburg for their financial assistance.

Appendix A. Supplementary data

Supplementary data (Additional sensing graphs of methanol, ethanol, acetone, and 3-pentanone and their corresponding calibration lines) to this article can be found online at https://doi.org/10.1016/j.rinp.2023.106864.

References

[1] Mirzaei A, Leonardi SG, Neri G. Detection of hazardous volatile organic compounds (VOCs) by metal oxide nanostructures-based gas sensors. Ceram Int 2016;42:15119.
[2] Malepe L, Ndinteh D, Mamo MA. The effect of measurement parameters on the performance of the sensors in the detection of organic compound vapours. Chem Phys Impact 2022;4:100068.
[3] Zhang H, Luo Y, Zhuo M, Yang T, Liang J, Zhang M, et al. Diethylamine gas sensor using V_2O_5-decorated α-Fe_2O_3 nanorods as sensing material. RSC Adv 2016;6:6511–5.
[4] Li L, Li J, Meng T, Liu Z, Zhou H, Zhu J, et al. Diethylamine fluorescence sensor based on silica hollow sphere photonic crystals. Anal Methods 2021;13:2189–95.
[5] Sun Li, Rotaru A, Robeyns K, Garcia Y. A colorimetric sensor for the highly selective, ultra-sensitive, and rapid detection of volatile organic compounds and hazardous gases. Ind Eng Chem Res 2021;60(24):8788–98.
[6] Sun L, Wang B, Wang Y. High-temperature gas sensor based on novel Pt single atoms@SnO_2 nanorods@SiC nanosheets multi-heterojunctions. ACS Appl Mater Interfaces 2020;12:21808–17.
[7] Nikfarjam A, Hosseini S, Salehifar N. Fabrication of a highly Sensitive single aligned TiO_2 and gold nanoparticle embedded TiO_2 nano-fiber gas sensor. ACS Appl Mater Interfaces 2017;9:15662–71.
[8] Kumar R, Al-Dossary O, Kumar G, Umar A. Zinc oxide nanostructures for NO_2 gas–sensor applications: A review. Nano-Micro Lett 2015;7(2):97–120.

[9] Najim AA, Shaker SS, Muhi MAH. Room temperature NO_2 gas sensor based on SnO_2-WO_3 thin films. Plasmonics 2017;12(4):1051–5.

[10] Bigiani L, Zappa D, Maccato C, Comini E, Barreca D, Gasparotto A. Quasi-1D MnO_2 nanocomposites as gas sensors for hazardous chemicals. Appl Surf 2020;512:145667.

[11] Xiao J, Liu P, Liang Y, Li BH, Yang GW. High aspect ratio β-MnO_2 nanowires and sensor performance for explosive gases. J Appl Phys 2013; 114: 073513.

[12] Shinde PV, Xia QX, Ghule BG, Shinde NM, Seonghee J, Kim KH, et al. Hydrothermally grown α-MnO_2 interlocked mesoporous micro-cubes of several nanocrystals as selective and sensitive nitrogen dioxide chemoresistive gas sensors. Appl Surf Sci 2018;442:178–84.

[13] Umar A, Ibrahim AA, Kumar R, Algadi H, Albargi H, Ahmad F, et al. α-MnO_2 nanowires as potential scaffolds for a high-performance formaldehyde gas sensor device. Coatings 2021;11:860.

[14] Okechukwu VO, Mavumengwana V, Hümmelgen IA, Mamo MA. Concomitant in situ FTIR and impedance measurements to address the 2-methylcyclopentanone vapour-sensing mechanism in MnO_2-polymer nanocomposites. ACS Omega 2019;4:8324–33.

[15] Umar A, Ibrahim AA, Kumar R, Albargi H, Zeng W, Alhmami MAM, et al. Gas sensor device for high-performance ethanol sensing using α-MnO_2 nanoparticles. Mater Lett 2021;286:129232.

[16] Olifant GE, Mavumengwana V, Hümmelgen IA, Mamo MA. Understanding the sensing mechanism of carbon nanoparticles: MnO_2–PVP composites sensors using in situ FTIR—Online LCR meter in the detection of ethanol and methanol vapor. J Mater Sci Mater Electron 2019;30:3552–62.

[17] Malepe L, Ndungu P, Ndinteh DT, Mamo MA. Nickel oxide-carbon soot-cellulose acetate nanocomposite for the detection of mesitylene vapour: Investigating the sensing mechanism using an LCR meter coupled to an FTIR spectrometer. Nanomaterials 2022;12:727.

[18] Xing Y, Wang Z, Zhu Y, Yan J, Chen Y. High-performance chlorobenzene sensor of bimetallic ZIF-8(Zn@Co) based one-dimensional photonic crystals. Phys Lett A 2021;400:127301.

[19] Drobek M, Kim J, Bechelany M, Vallicari C, Julbe A, Kim SS. MOF-based membrane encapsulated ZnO nanowires for enhanced gas sensor selectivity. ACS Appl Mater Interfaces 2016;8:8323–8.

[20] Tian H, Fan H, Li M, Ma L. Zeolitic imidazolate framework coated ZnO nanorods as molecular sieving to improve selectivity of formaldehyde gas sensor. ACS Sens 2016;1(3):243–50.

[21] Matatagui D, Sainz-Vidal A, Gràcia I, Figueras E, Cané C, Saniger JM. Chemoresistive gas sensor based on ZIF-8/ZIF-67 nanocrystals. Sens Actuat: B Chem 2018;274:601–8.

[22] Zhang J, Guo J, Xu H, Cao B. Reactive-template fabrication of porous SnO_2 nanotubes and their remarkable gas-sensing performance. ACS Appl Mater Interfaces 2013;5(16):7893–8.

[23] Fu N, Ren X. Synthesis of double-shell hollow TiO_2@ZIF-8 nanoparticles with enhanced photocatalytic activities. Front Chem 2020;8:578847.

[24] Greenshields MWCC, Hümmelgen IA, Mamo MA, Shaikjee A, Mhlanga SD, van Otterlo WAL, et al. Composites of polyvinyl alcohol and carbon (coils, undoped and nitrogen doped multiwalled carbon nanotubes) as ethanol, methanol and toluene vapor sensors. J Nanosci Nanotechnol 2011;11(11):10211–8.

[25] Olifant GE, Kondiah K, Mamo MA. Application of candle soot CNPs-TiO_2-PVP composite in the detection of volatile organic compounds with aldehyde, amine and ketone functional groups by resistance and impedance responses. Nano Express 2021;2(2):020010.

[26] Wan X, Yang S, Cai Z, He Q, Ye Y, Xia Y, et al. Facile synthesis of MnO_2 nanoflowers/N-doped reduced graphene oxide composite and its application for simultaneous determination of dopamine and uric acid. Nanomaterials 2019;9:847.

[27] Wu C, Liu Q, Chen R, Liu J, Zhang H, Li R, et al. Fabrication of ZIF-8@SiO_2 micro/nano hierarchical superhydrophobic surface on AZ31 magnesium alloy with impressive corrosion resistance and abrasion resistance. ACS Appl Mater Interfaces 2017;9:11106–15.

[28] Tailor R, Vijay YK, Bafna M. Carbon Soot Polymer Nanocomposites (CSPNCs): production, surface morphological, glass transition temperature phenomenon and optical properties, environmental emissions. London, United Kingdom: IntechOpen; 2020 [Online]. Available: https://www.intechopen.com/chapters/72386.

[29] Jaganyi D, Altaf M, Wekesa I. Synthesis and characterization of whisker-shaped MnO_2 nanostructure at room temperature. Appl Nanosci 2013;3(4):329–33.

[30] Guo H, Zhang Z, Jiang Z, Chen M, Einaga H, Shangguan W. Catalytic activity of porous manganese oxides for benzene oxidation improved via citric acid solution combustion synthesis. J Environ Sci 2020;98:196–204.

[31] Zhang Y, Qin Z, Wang G, Zhu H, Dong M, Li S, et al. Catalytic performance of MnO_x–NiO composite oxide in lean methane combustion at low temperature. Appl Catal B 2013;129:172–81.

[32] Sun S, Yang Z, Cao J, Wang Y, Xiong W. Copper-doped ZIF-8 with high adsorption performance for removal of tetracycline from aqueous solution. J Solid State Chem 2020;285:121219.

[33] Tang M, Wang Z, Wang D, Mao R, Zhang H, Xu W, et al. Construction of LaF_3 QD-modified SnS_2 nanorod composites for ultrasensitive detection of H_2S. J Mater Chem A 2023;11:9942–54.

[34] Tang M, Zhang D, Chen Q, Wang Z, Wang D, Yang Z, et al. Heterostructure construction of SnS_2 Debye nanowires modified with ZnO nanorods for chemiresistive H_2S detection in sulfur hexafluoride decomposition products. Sens Actuators, B 2023;390:133952.

[35] Zhang D, Yu S, Wang W, Huang J, Pan W, Zhang J, et al. UV illumination-enhanced ultrasensitive ammonia gas sensor based on (001)TiO2/MXene heterostructure for food spoilage detection. J Hazard Mater 2022;423:127160.

[36] Zhang D, Luo Y, Huang Z, Tang M, Sun J, Wang X, et al. Ultrathin coordination polymer nanosheets modified with carbon quantum dots for ultrasensitive ammonia sensors. J Colloid Interface Sci 2023;630:776–85.

[37] Wang J, Yang P, Wei X. High-performance, room-temperature, and no-humidity-impact ammonia sensor based on heterogeneous nickel oxide and zinc oxide nanocrystals. ACS Appl Mater Interfaces 2015;7:3816–24.

[38] Song Z, Wei Z, Wang B, Luo Z, Xu S, Zhang W, et al. Sensitive room-temperature H_2S gas sensors employing SnO_2 quantum wire/reduced graphene oxide nanocomposites. Chem Mater 2016;28:1205–12.

[39] Tan CK, Blackwood DJ. Interactions between polyaniline and methanol vapour. Sens Actuators B 2000;71(3):184–91.

[40] Hirayama K, Sakai Y, Kameoka K, Noda K, Naganawa R. Preparation of a sensor device with specific recognition sites for acetaldehyde by molecular imprinting technique. Sens Actuators B 2002;86(1):20–5.

[41] Bai H, Shi G. Gas sensors based on conducting polymers. Sensors 2007;7:267–307.

[42] Zhang J, Boyd A, Tselev A, Paranjape M, Barbara P. Mechanism of NO2 detection in carbon nanotube field effect transistor chemical sensors. Appl Phys Lett 2006;88(12):123112.

[43] Li Z, Li H, Wu Z, Wang M, Luo J, Torun H, et al. Advances in designs and mechanisms of semiconducting metal oxide nanostructures for high-precision gas sensors operated at room temperature. Mater Horiz 2019;6:470–506.

[44] Dey A. Semiconductor metal oxide gas sensors: A review. Mater Sci Eng B 2018;229:206–17.

[45] Wang D, Zhang D, Guo J, Hu Y, Yang Y, Sun T, et al. Multifunctional poly(vinyl alcohol)/Ag nanofibers-based triboelectric nanogenerator for self-powered MXene/tungsten oxide nanohybrid NO2 gas sensor. Nano Energy 2021;89:106410.

[46] Wang D, Zhang D, Yang P, Mi YQ, Zhang J, Yu L. Multifunctional latex/polytetrafluoroethylene-based triboelectric nanogenerator for self-powered organ-like MXene/Metal–Organic Framework-derived CuO nanohybrid ammonia sensor. ACS Nano 2021;15:2911–9.

[47] Barsan N, Simion C, Heine T, Pokhrel S, Weimar U. Modeling of sensing and transduction for p-type semiconducting metal oxide based gas sensors. J Electroceram 2010;25(1):11–9.

[48] Pandeeswari R, Sonia T, Balamurugan D, Jeyaprakash BG. Highly selective dimethylamine vapour sensors based on spray deposited β-Bi_2O_3 nanospheres at low temperature. Sens Imaging 2022;23:1.

[49] Atamny F, Blocker J, Du Botzky A, Kurt H, Timpe O, Loose G, et al. Surface chemistry of carbon: Activation of molecular oxygen. Mol Phys 1992;76:851–86.

[50] Isokoski K, Poteet CA, Linnartz H. Highly resolved infrared spectra of pure CO2 ice (15–75 K). Astron Astrophys 2013;555:A85.

[51] Schadle T, Pejcic B, Mizaikoff B. Monitoring dissolved carbon dioxide and methane in brine environments at high pressure using IR-ATR spectroscopy. Anal Methods 2016;8:756–62.

[52] Baratta GA, Palumbo ME. The profile of the bending mode band in solid CO_2. Astron Astrophys 2017;608:A81.